

Controlling Defects in Continuous 2D GaS Films for High Performance Wavelength-Tunable UV-Discriminating Photodetectors

Yang Lu,¹ Jun Chen,¹ Tongxin Chen,¹ Yu Shu,¹ Ren-Jie Chang,¹ Yuewen Sheng,¹ Viktoryia Shautsova,¹ Nhlakanipho Mkhize,¹ Philip Holdway,¹ Harish Bhaskaran,¹ Jamie H. Warner^{1}*

¹Department of Materials, University of Oxford, Parks Road, Oxford, OX1 3PH, United Kingdom

*jamie.warner@materials.ox.ac.uk

Keywords: Gallium sulfide, CVD, stability, degradation, defects, large bandgap 2D semiconductor, photodetectors

Abstract:

We developed a CVD method for thickness-controlled (1–4L), uniform and continuous films of both defective GaS_{0.87} and stoichiometric GaS. We studied the unique degradation mechanism of GaS_{0.87} with XPS and ADF-STEM, and found that the poor stability and weak optical signal from GaS is strongly related to photo-induced oxidation at defects. An enhanced stability of the stoichiometric GaS was demonstrated under laser and strong UV lights, and by controlling defects in GaS, the photoresponse range could be changed from vis-to-UV to UV-discriminating. The stoichiometric GaS is suitable for large-scale UV-sensitive high-performance photodetector arrays for information encoding under large vis-light noise, with short response time (< 66 ms), excellent UV photoresponsivity (4.7 A/W for trilayer GaS) and 26-times increase of signal-to-noise compared with small bandgap 2D semiconductors. By comprehensive characterizations from atomic-scale structures to large-scale device performances in 2D semiconductors, we provide insights into the role of defects, importance of neglected material-quality control and how to

enhance device performance, and both layer-controlled defective GaS_{0.87} and stoichiometric GaS prove to be promising platforms for study of novel phenomena and new applications.

Introduction

Two-dimensional (2D) semiconductors have shown great potential in next-generation electronics and optoelectronics due to its extraordinary thickness-dependent properties.¹⁻⁴ The applications in increasingly extensive fields demand the discovery of novel 2D semiconductors with particular properties.⁵⁻¹¹ For example, most 2D semiconductors that have been studied possess small bandgaps, while the applications for 2D LEDs with blue or ultraviolet (UV) light emission, formation of van der Waals type-I heterojunctions and quantum wells call for materials with a larger bandgap.¹²⁻¹⁴ Gallium (II) sulfide (GaS), a member of the group-III monochalcogenide layered materials, is one such semiconductor with a wide bandgap semiconductor but scarcely explored.¹⁵⁻¹⁶ Bulk GaS has a bandgap of ~2.5 eV, and its bandgap increases with decreasing thickness due to quantum confinement effects, which gives wide tunability that could fill in the vacuum between 2D small bandgap semiconductors and insulators.¹⁷⁻¹⁸ Previous reports of mechanically-exfoliated few-layer GaS devices have demonstrated high photoresponsivity up to 64.43 A/W, large on/off ratios (10^4 – 10^5) and short response time of < 10 ms, which is suitable for many applications including photodetector, photoswitching and flexible devices.¹⁹⁻²⁰

Other issues that come with the extending study of 2D materials are questions related to their stabilities in ambient environment.²¹⁻²² The stability of a material is not only the interior crucial factor in applications that limits the device's working environment and lifetime, but should also be a preliminary knowledge for further scientific study to avoid misinterpretation. Studies concerning the ambient stability of 2D materials (mainly involving oxidation) have been focused on several well-developed 2D materials, and they can be generally categorized by stability into

three: 1) Generally stable (graphene, h-BN, MoS₂, WS₂, etc.) Owing to the absence of dangling bonds, these surfaces are considered as immune to oxidation, but the defects and grain boundaries are more reactive as they can provide reactive bonding sites and may reduce the kinetic barrier for O₂ dissociation.²³⁻²⁶ 2) Reactive to air (silicene, germanene, MoTe₂, etc.). It was shown that the oxidation kinetic barrier is zero for silicene surface and the process should be spontaneous.²⁷⁻²⁹ 3) Photo-induced oxidation (black phosphorus, CrI₃, etc.). These 2D materials usually degrade slowly in air but the process can be greatly accelerated by light.³⁰⁻³¹ For example, CrI₃ degrades under illumination by Cr³⁺ d-d transitions induced ligand substitution into Cr(H₂O)₆³⁺.³² The degradation of some members of the layered Ga-family has been studied. Jannatul et al. used Raman spectroscopy to show that both Te metals and tellurium oxides forms on the surface of layered GaTe crystals due to rapid oxidation.³³ Recently, Zhao et al. demonstrated that GaSe began to degrade within hours on exposure to air into amorphous selenium, Ga₂Se₃ and Ga₂O₃.³⁴ However, the degradation chemistry for each material is different, and more studies are needed for the increasing new members of 2D family.

Although there have been a few studies on thin GaS crystals, the stability of GaS is still in question, which greatly hindered its further studies. On one hand, GaS shows no obvious morphology changes in ambient environment for months. On the other hand, many researches have noticed that few-layer GaS devices suffered from poor long-term performance and optical signals were considerably weak in some studies,^{19, 35} which impede further application of the material in optics or optoelectronics. In addition, due to difficulties in exfoliation and lack of thickness-controlled synthesis methods, previous reports were unable to study layered-dependent properties of the 2D layered material, and to our knowledge, characterization or properties of GaS less than 3 layers are missing. Furthermore, although other members in the group-III monochalcogenide layered

materials with similar structures (GaSe, GaTe, InSe) have attracted intense attention as they have demonstrated superior optical properties including ultra-high second-harmonic generation,³⁶⁻³⁷ giant piezo-phototronic response,³⁸ polarization-dependent absorption,³⁹ etc.,⁴⁰⁻⁴¹ properties of GaS with wide potential remain unexplored as a result of unanswered stability issues and unsatisfying samples. Recently, our group have developed a simple and atmospheric-pressure chemical vapor deposition (CVD) method for growth of 2D GaS crystals,³⁵ which paved way for further study of the material's stability and layer-dependent properties.

Here we demonstrate large-area synthesis of thickness-controlled continuous films (1–4L) of defective GaS_{0.87} and defect-free GaS crystals by our optimized CVD synthesis method. The elemental composition was determined by energy-dispersive X-ray spectroscopy (EDX) and X-ray photoelectron spectroscopy (XPS). A comprehensive characterization of the defective GaS_{0.87} and stoichiometric GaS crystals was conducted by means of Raman spectrometry, atomic force microscopy (AFM) and scanning electron microscopy (SEM). To answer the question of GaS stability, the degradation behavior of the two crystals under laser and UV light were compared and the unique degradation mechanism was studied by valence state changes with XPS, atomic structure changes with high angle annular dark field scanning transmission electron microscopy (HAADF-STEM) and further linked with device performance, and we found that the poor stability and weak optical signal from GaS is strongly related to defects. Finally, the material-based photodetectors showed excellent UV detection ability (with highest $R=10.2$ A/W, $D^*=1.6\times 10^{12}$ Jones, EQE=2364% and photoresponse time < 66 ms), and by tuning defects in GaS, the photoresponse range could be changed from vis-to-UV to UV-discriminating. We also demonstrated the application of large-scale and uniform GaS high-performance devices for information encoding, with great stability and sensitivity to UV light signals even under large

visible light background. Thus, the comprehensive study of defects could give a deeper understanding of its role in 2D materials, and could lead to the discovery of novel phenomena in GaS such as non-linear properties which was difficult due to neglected material-quality control, and also presents a valuable insight for enhancing 2D device performance.

Results and discussion

The defects in GaS material was tuned in our CVD system for further study of their influence on material properties and device performance. Figure 1a-d shows the schematic illustration of the synthesis of two GaS crystals, defective $\text{GaS}_{0.87}$ and stoichiometric GaS (the stoichiometry was determined in later discussion). For the synthesis of the former one (Fig. 1a), gallium (III) sulfide (Ga_2S_3) powder was used as the single-source precursor with the substrate (silicon with 300 nm oxide layer on top) placed downstream at a lower temperature zone. 100 sccm 25% H_2/Ar mix gas was used as the carrier gas throughout the synthesis. The system is first flushed for 30 min, and then the furnace is heated up at 40 °C/min to 810 °C and maintained for 20 min before fast cooling with pure Ar flow (Fig. 1c). Similar setups are used for the synthesis of stoichiometric GaS (Fig. 1b&d). A separate furnace (denoted as Furnace 1) is added to the upstream of the system with 20 mg sulfur powder in the center of it, and the setup of the original furnace (denoted as Furnace 2) remains unchanged. The operation procedures are kept the same except for ramping up Furnace 1 as Furnace 2 reaches 570 °C, so that both furnaces achieve the designated temperature at the same time (Furnace 1: 120 °C, Furnace 2: 810 °C). After 20 min of reaction, both furnace are opened for fast cooling at the same time.

The relations between morphology and synthesis parameters are first studied for both defective $\text{GaS}_{0.87}$ and defect-free GaS, which have many in common. As the deposition amount increases, the morphology changes from isolated monolayer triangles with rounded corners, to monolayer

continuous films, to bilayer continuous films, further to trilayer films with adlayers (small bulk crystals) on top of the film, and films with the thickness of 4 layers (Figure 1e-f) can be achieved in defective $\text{GaS}_{0.87}$. With fine control of the growth conditions, we can achieve large-area and uniform all-monolayer continuous films throughout the substrate. As can be seen in Figure 1g, the two very sides of substrate show isolated monolayer GaS domains due to smaller flow rate near the side of the system, but the major area (almost the whole substrate) is covered with monolayer continuous film. The film thicknesses are determined by AFM results and Raman peak positions, which will be discussed later. Besides, the growth behavior is self-limiting in nature as the film thickness is highly uniform for very large areas. The lack of contrast variation in SEM and AFM images (Fig. 1e-g, Fig. 3a&c) indicates that there are no adlayers on any of the monolayer and bilayer regions. AFM results also show that even for the 3 and 4 layer films, the film roughness of regions between small bulk crystals is only 0.22 nm (Fig. S1a-b), hence the morphology can be described as “some small islands of GaS crystals sitting epitaxially on top of a large area continuous 3–4 layer GaS 2D films”. This layer-controlled synthesis is essential for studying its layer-dependent properties. Moreover, the deposition rate (which can be estimated by film thickness given the same deposition time) increases as the substrate temperature decreases. We also noticed that the deposition rate increases with increasing temperature of precursor (i.e. the sublimation rate of precursor) (See Figure S2). Taking the growth of defective $\text{GaS}_{0.87}$ as an example, growing at 650 °C for 20 min resulted in isolated domains of monolayer defective $\text{GaS}_{0.87}$, and as the reaction time extends, it would continue to merge into monolayer continuous films. At lower reaction temperature of 637 °C, the deposition amount increases and the film is mostly bilayer, followed by 3–4 layer film at 625 °C. This suggests that the growth kinetics are controlled by the deposition stage. Finally, the addition of sulfur could greatly increase the deposition rate

for stoichiometric GaS compared with defective $\text{GaS}_{0.87}$. At 650 °C, stoichiometric trilayer GaS film forms instead of monolayer defective $\text{GaS}_{0.87}$ with the addition of sulfur, and monolayer stoichiometric GaS is obtained at a growth temperature of 675 °C.

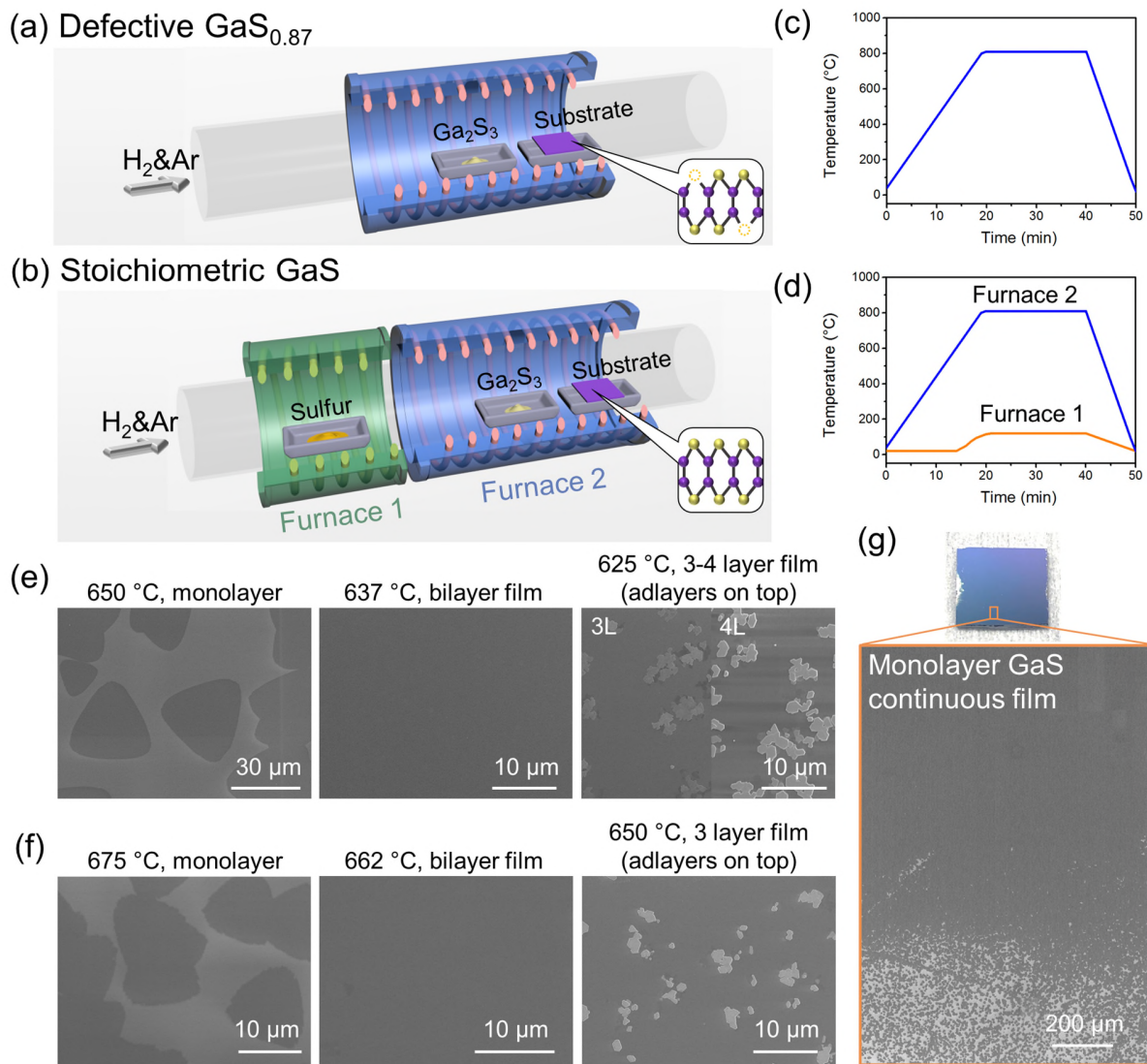


Figure 1. Synthesis and SEM images of gallium (II) sulfide: (a, b) Schematic of synthesis of defective $\text{GaS}_{0.87}$ and stoichiometric GaS, respectively. (c, d) Temperature profile for the process of $\text{GaS}_{0.87}$ and GaS growth, respectively. (e) SEM images of defective $\text{GaS}_{0.87}$ from monolayer to 4 layer films. (f) SEM images

of stoichiometric GaS from monolayer to 3 layer films. (g) Photograph and SEM images of synthesized large-area uniform monolayer stoichiometric GaS continuous films.

Next, to further check the stoichiometry information on the materials, both EDX and XPS were employed to characterize the gallium (II) sulfide films. As shown in Figure 2a, the Ga and S element peaks can be clearly identified in EDX. The two peaks are fitted and statistical results for the samples are summarized in Table 1. The values are narrowly distributed and consistent for crystals from bulk to monolayer, indicating that it is not related to surface effects or caused by byproducts, but intrinsic stoichiometry of the material. A S:Ga ratio of 0.87 ± 0.03 was obtained for defective GaS films, and the stoichiometric GaS shows the pristine stoichiometry of 1.00 ± 0.01 . XPS was further conducted as a supplementary to EDX, which is shown in Figure 2b-c. The Ga 3d peak at 20.43 ± 0.05 eV was used for quantification of Ga elements, and the other two fitted peaks located at 162.7 eV (S 2p_{3/2}) and 163.8 eV (S 2p_{1/2}) were used for quantification of S elements. The obtained results from XPS were in great accordance with EDX, with a S:Ga ratio of 0.88 for defective GaS and 1.01 for stoichiometric GaS. Hence, according to the well-agreed EDX and XPS results, the defective and stoichiometric 2D crystals are denoted as GaS_{0.87} and GaS, respectively.

These results showed that the addition of sulfur have significant influence on the composition of the final crystal. Unlike many well-studied TMD materials where the product has only one stoichiometry, the cases with III(A) group metals (Ga, In) are more complicated than them based on our experiments. A detailed discussion of the precursor Ga₂S₃, the catalyst effect of H₂ and the rate-limiting step in GaS growth is provided in Supporting information, and the reaction mechanism is illustrated in Fig. 2d: Step 1. Ga₂S₃ is decomposed into volatile Ga* (a gallium-containing species) and H₂S, catalyzed by hydrogen; Step 2. The sublimated Ga* and H₂S in gas

phase (labeled with (g)) are transported to the substrate; Step 3. A balance of absorption and desorption of $\text{Ga}^*(\text{g})$ and $\text{H}_2\text{S}(\text{g})$ is established on the surface, with the absorbed amount of Ga^* and H_2S (labeled with (a)) determined by substrate temperature and gas phase concentration. Step 4. $\text{Ga}^*(\text{a})$ and $\text{H}_2\text{S}(\text{a})$ react to form GaS_x with various stoichiometry. Among these steps, step 4 is considered as the rate-limiting step, and thus the relative ratio of the absorbed species $\text{Ga}^*(\text{a})$ and $\text{H}_2\text{S}(\text{a})$ determines the stoichiometry in the final product. As H_2S molecules are lighter (indicating smaller van der Waals interaction) and has no special bindings with the substrate, there should be less $\text{H}_2\text{S}(\text{a})$ absorbed than $\text{Ga}^*(\text{a})$ given the same concentration. Hence, even the S:Ga stoichiometry from the precursor is 1.5, the actual absorbed species on the substrate have a much smaller S:Ga ratio. The influence from this is illustrated in Figure 2e-g. When H_2S only comes from the precursor and is deficient, a defective yet thermally stable 2D crystal $\text{GaS}_{0.87}$ is formed, which has the same crystal structure of GaS but with ~13% sulfur vacancies. When suitable amount of H_2S is added to the system, the ratio of S:Ga in reactive species becomes larger and stoichiometric GaS is formed. If more H_2S is continuously added to the gas phase, extra sulfur on the substrate resulted in the formation of 2D Ga_2S_3 (Table 1 & Fig. S3). The role of hydrogen was usually considered as creating reduction atmosphere, but our results suggest that Ga_2S_3 could form under such high hydrogen environment, and thus the real contribution of hydrogen is to facilitate the transformation of the precursors into active species (H_2S and Ga^*). Our findings suggest that extra care must be taken for 2D materials with other possible forms of stoichiometry, and especially in our case where it is not the stoichiometry in the precursor, but in the absorbed reactive species which determines that in the final product.

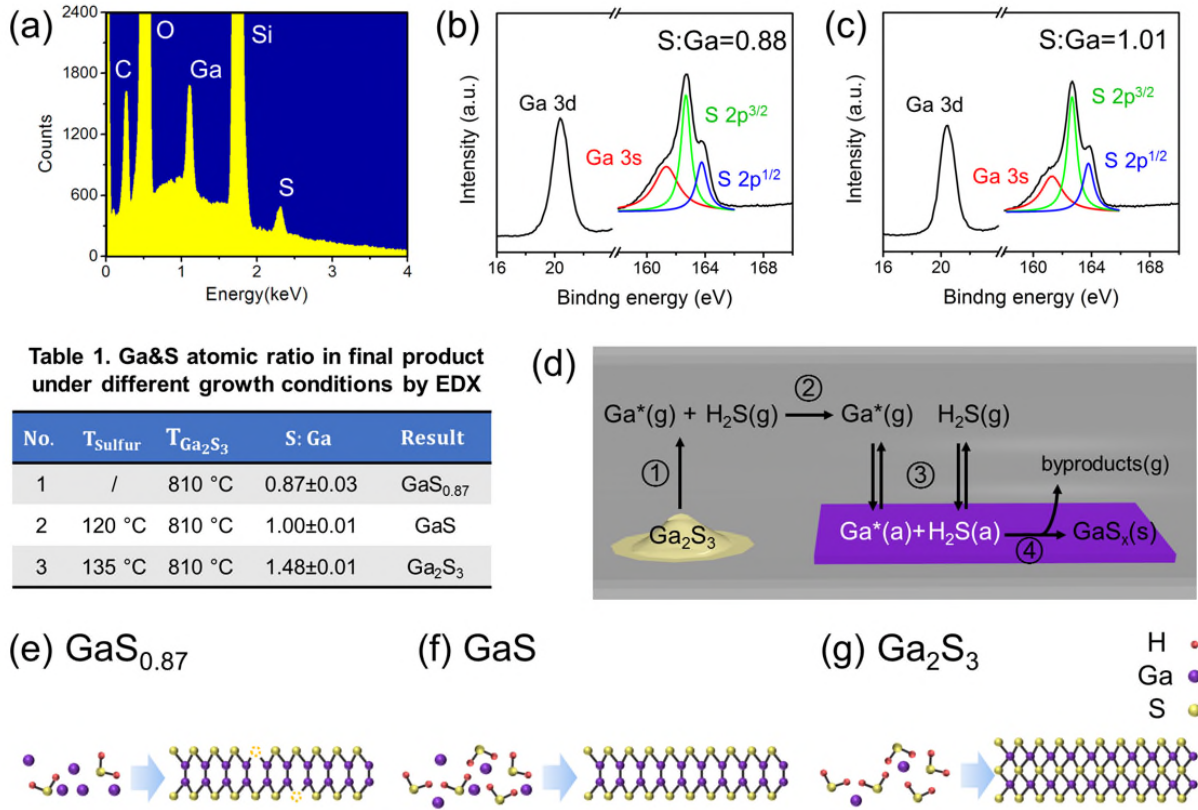


Figure 2. Stoichiometry and growth mechanisms for 2D layered Gallium Sulfide crystals: (a) EDX spectrum of a typical gallium sulfide thin films. (b, c) XPS spectrum of monolayer $\text{GaS}_{0.87}$ and GaS, respectively. (d) Schematic illustration of the reaction mechanisms. (e-g) The effect of relative ratio of absorbed species on the stoichiometry in the final product ($\text{GaS}_{0.87}$, GaS, Ga_2S_3).

Next, for the first time, we established a fast and easy approach for determining the number of layers of GaS by Raman spectroscopy as the starting point of GaS layer-dependent properties study. Bulk GaS has three Raman peaks, which are located at $187.3 \text{ cm}^{-1}(\text{A}_{1\text{g}})$, $294.1 \text{ cm}^{-1}(\text{E}_{1\text{g}})$, $360.2 \text{ cm}^{-1}(\text{A}_{1\text{g}})$ (Fig. S4a).⁴² The signals of the peaks weakened with the decrease of number of layers, and in few-layered GaS, the $\text{E}_{1\text{g}}$ peak can hardly be distinguished from the signal from Si substrate. No other signals are observed from our samples. We found that the peak position of $\text{A}_{1\text{g}}$ is a trusty indicator for simple and fast identification of the GaS thickness between 1~4 layers. AFM was

first employed which confirmed the thickness for 1~4L GaS_{0.87} to be 0.85 nm (1L), 1.6 nm (2L), 2.5 nm (3L), 3.4 nm (4L) (Fig. 3a-b); and 1~3L GaS to be 0.85 nm (1L), 1.6 nm (2L), 2.6 nm (3L) (Fig. 3c-d), which is in accordance with previous reports from mechanically exfoliated GaS.⁴² Raman spectrum of the samples are then correlated with AFM results, and A¹_{1g} peak position of both samples decreased with decreasing number of layers due to reduced interaction between layers, as is also observed in GaSe with similar structure.⁴² As shown in Figure 3e, the A¹_{1g} peak position of GaS_{0.87} is at 182.3 cm⁻¹ (1L), 184.2 cm⁻¹ (2L), 185.3 cm⁻¹ (3L), 186.3 cm⁻¹ (4L); and for GaS the peak position is at 183.5 cm⁻¹ (1L), 184.3 cm⁻¹ (2L), 185.4 cm⁻¹ (3L). We also found that the Raman signal intensities of GaS are significantly stronger than their counterparts of GaS_{0.87} (Fig. 3f). For example, monolayer GaS A¹_{1g} peaks are more than three times stronger than that of monolayer GaS_{0.87}, even slightly stronger than that of 3L GaS_{0.87}. The stronger Raman signals indicate better crystallinity and less defects, and as will be discussed next, the difference in stability also accounts for the difference in Raman signal intensities.

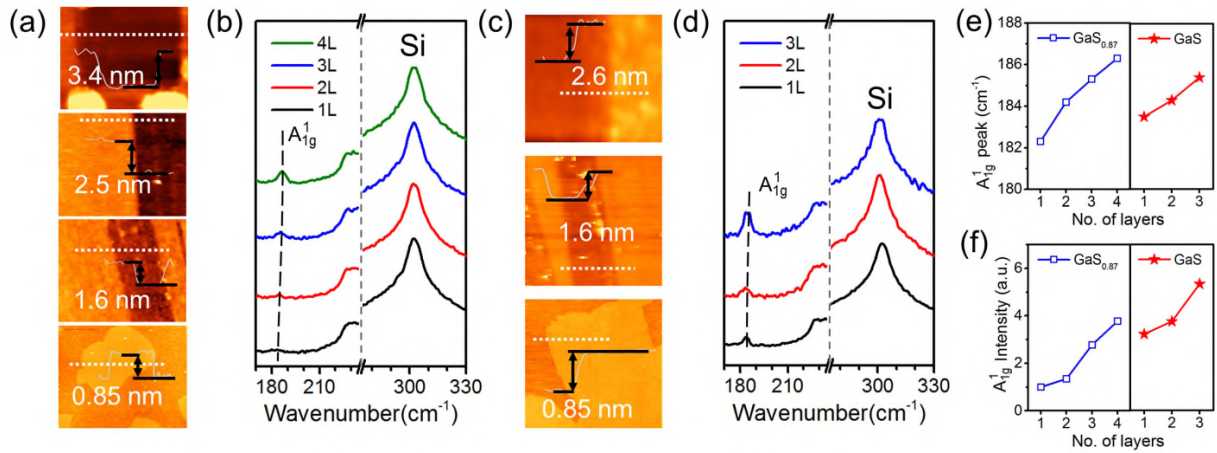


Figure 3. AFM image and Raman spectrum of gallium sulfide crystals: (a) AFM images of GaS_{0.87} films from monolayer to 4 layer and (b) corresponding Raman spectrum. (c) AFM images of GaS films from monolayer to 3 layer and (d) corresponding Raman spectrum. (e) Relation of A¹_{1g} peak position and film thickness. (f) Relation of A¹_{1g} peak intensity and film thickness.

As we mentioned before, the two gallium(II) sulfide samples ($\text{GaS}_{0.87}$ and GaS) are significantly different in stability under laser or UV light. Since Raman signals are related to the crystal's structure, the level of degradation from laser can be detected from the weakening of Raman peak signals due to loss of crystallinity or formation of new substances. Thus, the intensity of A_{1g} peak intensity can be used as an indicator of level of degradation, and in this work, the sample quality was always checked by Raman to be fresh before any further characterization was conducted. To study the effect of laser on the material, the evolution of Raman signal intensity from trilayer $\text{GaS}_{0.87}$ and GaS films with time were recorded every 3 seconds under 7.76 mW of 532 nm laser (spot size $\sim 1 \mu\text{m}$). As shown in Figure 4a, the Raman peak intensity in trilayer $\text{GaS}_{0.87}$ films started to decrease immediately and continuously until it dropped to only 20% of its starting value within 30 s. No peak shifting was observed, excluding the possibility of layer-by-layer laser-thinning. As a comparison, the trilayer GaS films showed more stable Raman signal intensities and after 30 s the signal was still above 80% of its original value. It is therefore believed that the lower Raman signals from $\text{GaS}_{0.87}$ films are also resulted from its instability under high-energy laser beam. Interestingly, unlike many other reports on the study of 2D materials degradation, in our experiments, apart from the changes in Raman signal intensities, little change was observed for the degraded gallium(II) sulfide. As can be seen from Figure 4c-e, AFM was used to acquire the topography of a region where the underlying 3L $\text{GaS}_{0.87}$ film had been annealed under 7.76 mW 532 nm laser for 60 s and no longer showed any signals from GaS or other substances (Fig. S5a, d). Such condition would usually generate a hole with the depth of the original film, whereas AFM height profile only showed a small 0.75 nm difference in height, even less than the thickness of monolayer GaS , indicating that the film was transformed into a non-volatile species without aggregation. The sample was also characterized by SEM but no difference was shown (Fig. S5c).

Raman mapping was used at the end of the series of characterizations to confirm the annealed region (Fig. S5b).

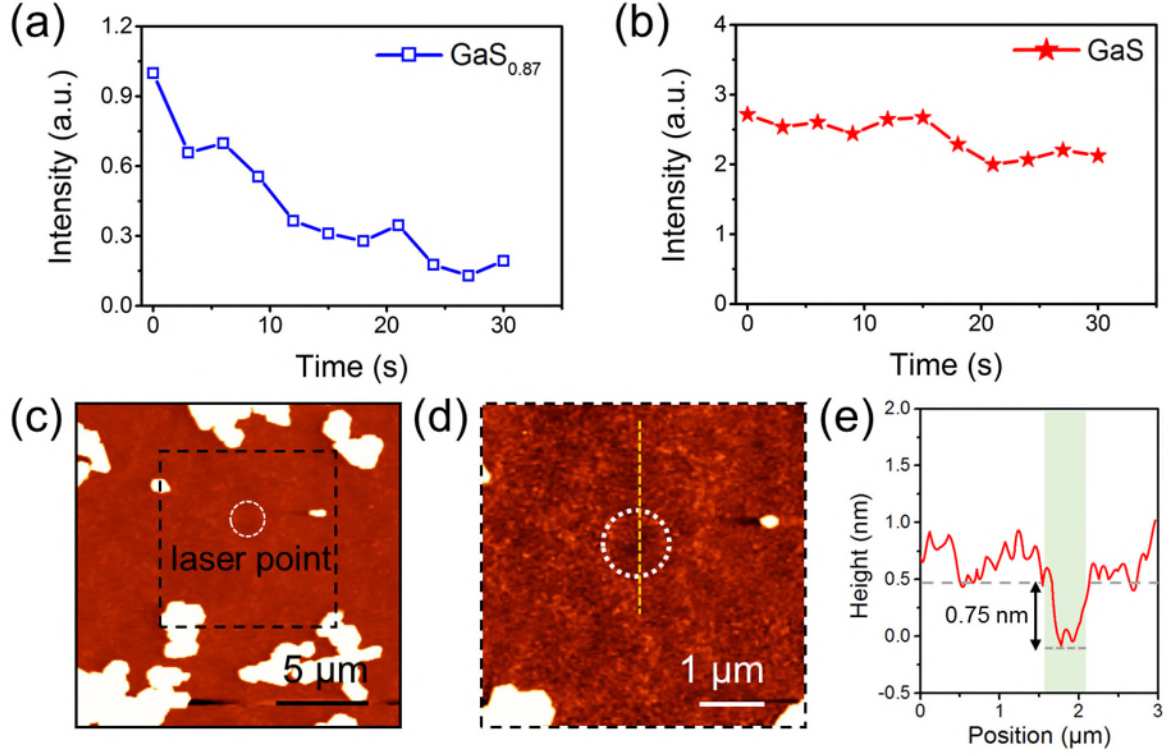


Figure 4. Laser-induced degradation of trilayer thin films of $GaS_{0.87}$. (a, b) Evolution in time of the A_{1lg} peak intensity in trilayer $GaS_{0.87}$ and trilayer GaS under 7.76 mW of 532 nm laser. (c, d) AFM image of trilayer $GaS_{0.87}$ films after annealed under 7.76 mW laser for 60 s. (e) AFM line profile of the annealed spot.

We then compared the optoelectronic properties of the crystals with different stoichiometry and studied the degradation of $GaS_{0.87}$ films under strong UV light. We used e-beam lithography for patterning and then 80 nm gold was deposited on top of it as electrode. As a large bandgap semiconductor, the off-state current of GaS is quite small. Therefore, the channel for 1L and 2L GaS (and $GaS_{0.87}$) films are designed to be 200 μm in width for larger current with 1 μm channel length, while the channel for the 3L and 4L GaS (and $GaS_{0.87}$) films are designed to be 20 μm in width, and we used SEM to exclude the devices with thick crystals sitting between the gaps so that

the properties we studied are related to the exact number of layers. To excite electrons from valence band into the conduction band, a 275 nm UV LED was used as the light source with intensities as high as 1.25 mW/cm². Figure 5a-f shows the photocurrent of the devices with different light intensities under a bias of 0–20V. Note that the photocurrent of 1L GaS_{0.87} was below our detection limit, which might have broken down during device fabrication or measurement. The 1–3 layer GaS and 2–4 layer GaS_{0.87} all showed good and sensitive photoresponse to the UV light. Photoresponsivity ($R = I_{\text{light}}/P$) is a critical parameter used to evaluate the sensitivity of the photodetector where I_{light} is photocurrent and P is the power of light illuminated in the channel. Another critical parameter used is external quantum efficiency ($\text{EQE} = hcR_{\lambda}/e\lambda$), which shows the number of electrons per incident photon, where h is the Planck's constant, c is the velocity of light, R_{λ} as the photoresponsivity at exciting photon wavelength λ . Based on these results, the photoresponsivity of each type of crystal was extracted and plotted in Figure 5i. We can see clearly that the photoresponsivity increases with the number of layers of the crystals due to increased absorption with thickness. The 4 layer GaS_{0.87} films achieved a high photoresponsivity of 10.2 A/W and high EQE of 2364% (@9.8 $\mu\text{W}/\text{cm}^2$), and 3 layer GaS film had a photoresponsivity of 4.7 A/W and EQE of 1312%, which is comparable to mechanically exfoliated GaS thin crystals, demonstrating the good quality of our synthesized GaS. In addition, the photoresponsivity of GaS crystals less than 3L is measured for the first time, with 1.1 A/W for 2L GaS at 9.8 $\mu\text{W}/\text{cm}^2$ ($\text{EQE} = 2.91 \times 10^{20}\%$), and 0.05 A/W for monolayer GaS at 102 $\mu\text{W}/\text{cm}^2$ ($\text{EQE} = 23\%$). Due to small dark current, gallium sulfide also showed good detectivity (D^*), which is used to describe the smallest detectable light signal:

$$D^* = \frac{R \times \sqrt{A}}{\sqrt{2eI_{\text{dark}}}}$$

where R is the photoresponsivity, A is the area of device channel, e as the electronic charge and I_{dark} as the dark current. A high D^* is measured for all our devices, with 1.6×10^{12} Jones for 4-layer $\text{GaS}_{0.87}$, 1.4×10^{12} Jones for 3-layer GaS and $\text{GaS}_{0.87}$, 5×10^{11} Jones for bilayer GaS , 6×10^{11} Jones for bilayer $\text{GaS}_{0.87}$ and 1.2×10^{11} Jones for monolayer GaS .

A comparative study of the photoresponse of bilayer and trilayer defective $\text{GaS}_{0.87}$ and stoichiometric GaS was also conducted as shown in Fig. 5g. We found that defective $\text{GaS}_{0.87}$ shows smaller photocurrent compared with stoichiometric GaS . Also, under weak light, the difference between two crystals was only 20-30%, but the gap increased with stronger light, and at a power density of $102 \mu\text{W}/\text{cm}^2$, the photoresponsivity of defective $\text{GaS}_{0.87}$ was less than half of the stoichiometric GaS , suggesting larger concentration of trap states in defective $\text{GaS}_{0.87}$. Another important difference lies in their behavior under strong UV light. As shown in Figure 5h-i, the I - t (current-time) curve, with the UV light of $1.25 \text{ mW}/\text{cm}^2$ switching on and off every 10 seconds, the stoichiometric GaS shows very stable and consistent performance with a sharp edge indicating instant response. The response time is less than 66 ms (Fig. S6), which is 2 to 3 orders less than other visible-light blind UV photodetectors (Table S1).⁴³⁻⁴⁹ However, the photocurrent of $\text{GaS}_{0.87}$ decreased drastically as soon as the light was on, and continued with every switching on of the light, dropping to only half of its starting values after only a total of 110 s exposure. Examination of the $\text{GaS}_{0.87}$ material after our device measurements under strong UV exposure showed very weak Raman signals (Fig. S7). Note that at lower power density ($102 \mu\text{W}/\text{cm}^2$) the $\text{GaS}_{0.87}$ devices showed stable performance (Fig. S8). Although the degradation of the $\text{GaS}_{0.87}$ devices were observed when bias was applied, it was not the result of large current flow or combined effect from current and light. As shown in Figure 5j, the device was first measured under weak UV light with stable performance, then excited with strong UV lights for 120 s with no bias applied. A clear drop

in current was shown which demonstrated that UV strong light alone can cause degradation in defective GaS_{0.87}. In comparison, stoichiometric GaS device was excited with strong UV lights for 15 min, and the photocurrent measured after that was still > 90% of its original values (Fig. 5k), demonstrating that the stoichiometric GaS was much more robust than the defective ones.

The wavelength dependent photoresponse of the two crystals was also studied by using a series of LEDs with different wavelengths from UV to visible red light at the same power density of 100 $\mu\text{W}/\text{cm}^2$. Both trilayer and bilayer GaS shows exclusive response to UV light, with no detectable photocurrent in the visible light range. However, the defective trilayer GaS_{0.87} showed response to blue light (470 nm), possibly from sub-bandgap states absorption arising from defects; and the bilayer GaS_{0.87} has rather weak photoresponse to 275 nm deep-UV light and its response to 370 nm or 470 nm is possibly below our detection limit. Based on the above results, the robust and UV-discriminating stoichiometric GaS crystals are very suitable for UV-sensitive applications.

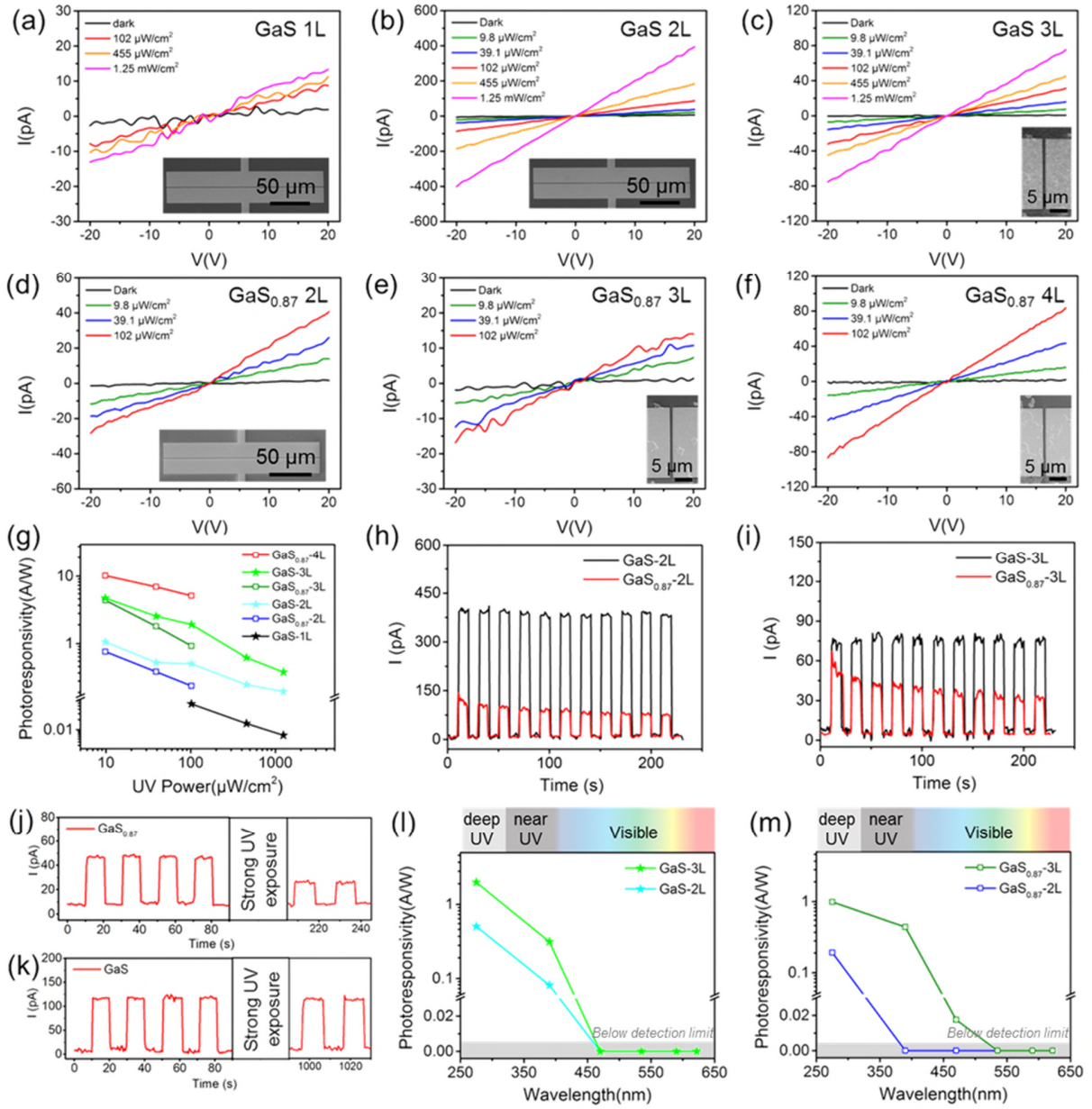


Figure 5. Optoelectronic performance of Gallium Sulfide thin films and UV-induced degradation behavior of $\text{GaS}_{0.87}$ films: (a-c) I-V curve of 1–3L stoichiometric GaS thin film devices under dark and different power densities of 275 nm UV light. Inset: SEM images of fabricated Au–GaS–Au devices. (d-f) I-V curve of 2–4L defective $\text{GaS}_{0.87}$ thin film devices under dark and different power densities of 275 nm UV light. Inset: SEM images of fabricated Au– $\text{GaS}_{0.87}$ –Au devices. (g) Power density dependence of photoresponsivity of CVD-grown large-scale GaS and $\text{GaS}_{0.87}$ thin film devices under UV light with a bias

of 20 V. (h) I-t curves of bilayer GaS_{0.87} and GaS thin film devices under 1.25 mW/cm² strong 275 nm UV light. (i) I-t curves of trilayer GaS_{0.87} and GaS thin film devices under 1.25 mW/cm² strong 275 nm UV light. (j) I-t curve of bilayer GaS_{0.87} thin film device's photoresponse to 102 μW/cm² 275 nm UV light before and after exposure to 1.25 mW/cm² strong 275 nm UV light for 120 s. (k) I-t curve of bilayer GaS thin film device's photoresponse to 102 μW/cm² 275 nm UV light before and after exposure to 1.25 mW/cm² strong 275 nm UV light for 900 s. (l) Wavelength dependence of photoresponsivity of 2–3L stoichiometric GaS thin film devices (100 μW/cm², 20V). (m) Wavelength dependence of photoresponsivity of 2–3L defective GaS_{0.87} thin film devices (100 μW/cm², 20V).

We further conducted a series of experiments to better understand the degradation behavior and mechanisms of the defective GaS_{0.87} under both high-intensity laser beam and high-energy UV lights using XPS and HAADF-STEM, respectively.

As shown in Figure 6a-b, we used 532 nm laser and a motorized stage to write a laser-annealed 200*200 matrix with a step size of 1 μm on monolayer GaS_{0.87} continuous film, with each spot being annealed for 1 s. XPS was then conducted on the region with a spot size of ~150 μm². Figure S9a-b shows that the annealed region presents no obvious difference with the unannealed region. However, XPS spectrum suggested loss of sulfur from the film as the S:Ga ratio reduced from 0.88 to 0.69 (Fig. 6c). In addition, the Ga 3d peak position also shifted from 20.3 eV to 20.89 eV, very close to the Ga 3d peak in Ga₂O₃, indicating possible oxidation reaction.⁵⁰⁻⁵¹ However, Raman spectrum of the annealed region showed no signals from Ga₂O₃ crystals.

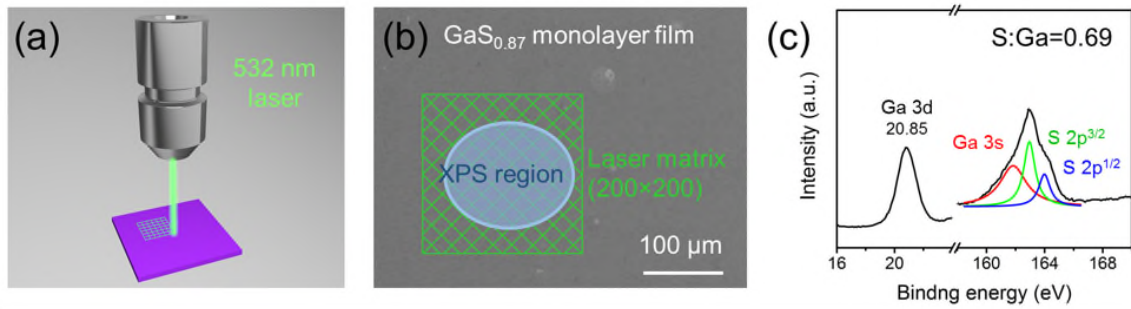
HAADF-STEM was further employed to look directly at the structure changes during degradation. The sample was prepared by direct growth of GaS_{0.87} crystals epitaxially on monolayer graphene films (Figure S10) that had been first transferred onto SiN TEM grids with 2 μm windows, similar to previous reports on GaSe.⁵² The monolayer GaS_{0.87} crystals are very sensitive to beam

irradiation and we focus on the study of bilayer and trilayer crystals which are stable under our characterization environment. Figure 6d shows the atomic structure of bilayer $\text{GaS}_{0.87}$ crystals with AA' stacking, where each corner of the hexagonal rings represents 2 S atoms and 2 Ga atoms, similar to our simulated results (Fig. 6f, Fig. S11). The graphene with low atomic number underneath the $\text{GaS}_{0.87}$ film is unable to see. Due to contaminations from CVD-grown graphene and polymer residues during transfer process, it was difficult to resolve every sulfur vacancy, however, certain sulfur vacancies in the lattice can be clearly seen in Figure 6e, in accordance with our proposed growth mechanisms. Then, the TEM grid was put under 1.25 mW/cm^2 strong 275 nm UV light for 15 min and put back to check for structure changes. Figure 6h is the enlarged image corresponding to the area shown in bilayer $\text{GaS}_{0.87}$ region in Figure 6g. As can be seen, in most areas the lattice were undamaged, and fast Fourier transform (FFT) image showed similar 6-fold symmetry patterns. However, disorder appeared in many nano-sized regions indicating degradation, and unlike the degradation in TMDs, there were no clusters. The formation of these nanoholes was instantly reflected by the impairment of optoelectronic properties shown in Figure 5h-j. In contrast, degradation in trilayer $\text{GaS}_{0.87}$ crystals are less obvious (Fig. 6i). After another 45 min of UV light illumination, the crystal disorder was much more serious. No hexagonal lattice can be observed from the original bilayer region shown in Figure 6k, and the broad ring-shaped FFT patterns suggest that the $\text{GaS}_{0.87}$ crystals have been transformed into certain amorphous phase. EDX was performed in the degraded region and no signal from S element was detected (Fig. 6k). Based on the elemental composition, the degraded substance is most likely to be amorphous Ga_2O_3 . In addition, Figure 6l showed that the trilayer $\text{GaS}_{0.87}$ crystals have not completely degraded yet. The 6-fold symmetry spots in FFT patterns became weaker and the same ring-shaped as in Figure 6k also appeared.

By combining the results from Figure 4 to 6, although the causes for degradation are different, it appears that the final products from laser and UV light damage are very similar to each other, as they both showed loss in sulfur elements, lack of crystallinity and absence of clusters. The degradation behavior of the defective $\text{GaS}_{0.87}$ are concluded as follows. First, the photo-induced degradation should start from the absorption of O_2 molecules at exposed S vacancy sites. Yang et al. showed that physisorbed O_2 molecules on monolayer GaS serve as acceptors of electron, which favors oxidation of GaS.²⁰ With the assist of either thermal energy from laser beam or being energized into excited state by UV light, the Ga atoms could be oxidized into Ga (III) to form Ga_xO_y , where the oxidization and loss of sulfur continue until it was transformed completely into amorphous Ga_2O_3 . This also explains why stoichiometric GaS crystals show greatly enhanced stability under laser and UV light. As a conjecture, the degradation could be greatly suppressed by encapsulation or inert gas protection, as have been shown to be effective in GaSe and GaTe.³⁴⁻³⁵ Second, the $\text{GaS}_{0.87}$ crystals degradation rate varies with thickness. After 1 hour exposure to strong UV light, the bilayer $\text{GaS}_{0.87}$ are completely destroyed while some lattice can still be observed in trilayer $\text{GaS}_{0.87}$. Similar degradation behavior is also noticed in laser-related experiments, where trilayer $\text{GaS}_{0.87}$ requires 30 s of annealing for the signals to disappear but monolayer $\text{GaS}_{0.87}$ requires less than 5 s, and we haven't noticed degradation in bulk GaS crystals. Amorphous Ga_2O_3 has been observed on the surface of gallium metals, where a less than 3 nm native oxide layer skin can prevent further oxidation of the inner metal.⁵³⁻⁵⁴ We suggest that the degraded amorphous Ga_2O_3 could behave in similar ways that slowed down further degradation underneath. In other words, the degradation is a surface sensitive phenomenon and is more pronounced with atomically thin GaS. This could be further applied to make atomically thick heterostructures. Third, the defective $\text{GaS}_{0.87}$ crystals, although having a large amount of sulfur vacancies (13%), are

surprisingly stable in ambient conditions. Samples after 8 months of storage in air showed little difference than fresh samples from every aspect, including optoelectronic properties. It should be investigated in the future whether these stable defects can be of use in optics, magnetism or other fields after proper protection from degradation. In summary, the degradation behavior of $\text{GaS}_{0.87}$ is quite unique in comparison with other 2D materials, and this could provide valuable information for other degradation studies.

Laser-induced degradation



UV-induced degradation

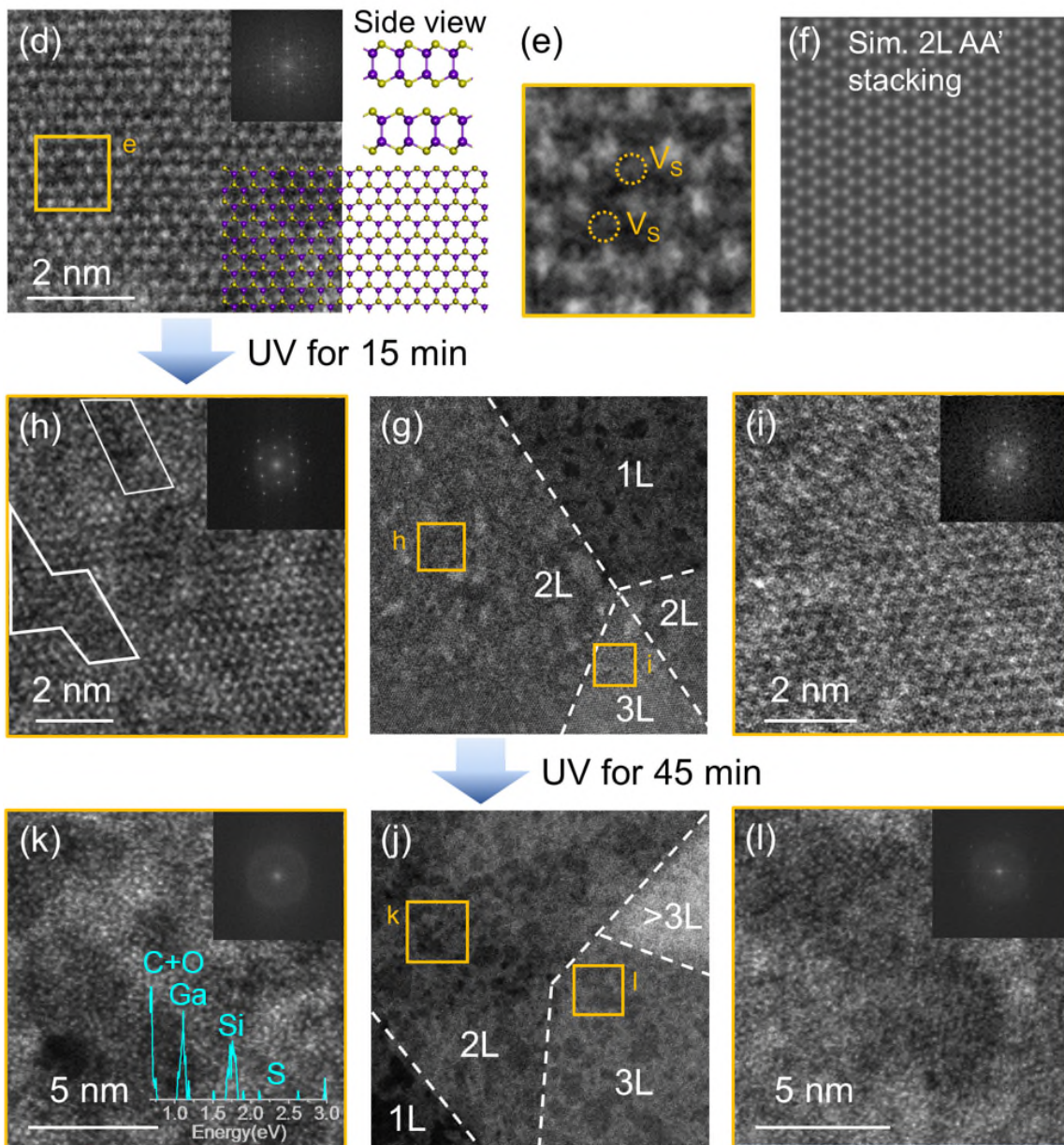


Figure 6. Degradation mechanisms of GaS_{0.87} films: (a) Schematics of matrix written by laser using motorized stage. (b) SEM image of monolayer GaS_{0.87} film after laser annealing and the position of XPS characterization. (c) XPS spectrum of monolayer GaS_{0.87} film after laser annealing. (d) HAADF-STEM image of bilayer AA' stacking GaS_{0.87} crystal. Inset: Corresponding FFT images of the figure. (e) Enlarged image of selected region showing sulfur vacancies. (f) Simulated bilayer AA' stacking GaS crystal. (g) HAADF-STEM image of GaS_{0.87} crystal after 15 min exposure to strong UV light. (h-i) Enlarged image from (g) of bilayer and trilayer GaS_{0.87} crystal after 15 min exposure to strong UV light. Inset: Corresponding FFT images of the area. (j) HAADF-STEM image of GaS_{0.87} crystal after another 45 min exposure to strong UV light. (k) Enlarged image from (j) of bilayer GaS_{0.87} crystal after 45 min exposure to strong UV light & EDX spectrum of the region showing no existence of S. Inset: Corresponding FFT images of the area. (l) Enlarged image from (j) of trilayer GaS_{0.87} crystal after 45 min exposure to strong UV light. Inset: Corresponding FFT images of the area.

Finally, owing to the unique UV-discriminating photoresponse, ultrashort response time, large on/off ratio, robustness and stable performance of the stoichiometric 2D GaS crystals, the device arrays are used for information encoding with UV lights, with the simplest design of 'on' state being '1' and 'off' state being '0'. As illustrated in Figure 7a, unlike most 2D crystals with small bandgap which would respond to both visible light and UV light, the large bandgap ensures that GaS crystals only shows large photocurrent when excited with UV lights, while no signal is detected when excited with visible light. The non-detectable photoresponse to strong and broadband white light LEDs (1.35 mW/cm², 400-700 nm) is shown in Figure 7b. Therefore, it is suitable for information encoding under noise of visible light/room light background, or be employed as a separate information receiving channel in addition to another broadband 2D semiconductor photodetector. Figure 7c shows the performance of bilayer GaS device's response to weak 65 μ W/cm² 275 nm UV light under simultaneous excitation with a strong 9.2 μ W 532 nm

green light laser (with a laser spot diameter of 5 μm). When there was green light only, the current was 5.8 pA. It increased to 66 pA under both green and UV light, hence gives a signal to noise ratio of 10.4. In comparison, the same condition was applied to monolayer MoS_2 , a most studied 2D optoelectronic material with a bandgap of 1.8 eV (See Figure S12&S13 for other characterizations of the monolayer MoS_2 device). It generated a large photocurrent of 0.95 μA with strong green light alone, and 1.35 μA under both green and UV light (Fig. 7d). The signal generated by UV light was immersed in the background signal from green light, giving a very low signal to noise ratio of 0.4. Therefore, by using large bandgap semiconductors, a 26-times increase of sensitivity was achieved for information encoding by UV light under large green light background. In addition, the response time of MoS_2 for UV light is ~ 41 s (due to photogating mechanism where minority carriers gradually transferred to interfaces or nearby molecules until saturation), while the response time of GaS is beyond our detection limit (< 66 ms), which is a critical advantage in high-speed information storage. The distinctive response to two different lights in these two materials also makes them good candidate for dual-channel information encoding, with GaS response only to deep-UV lights while MoS_2 response mainly to green light and little to UV lights.

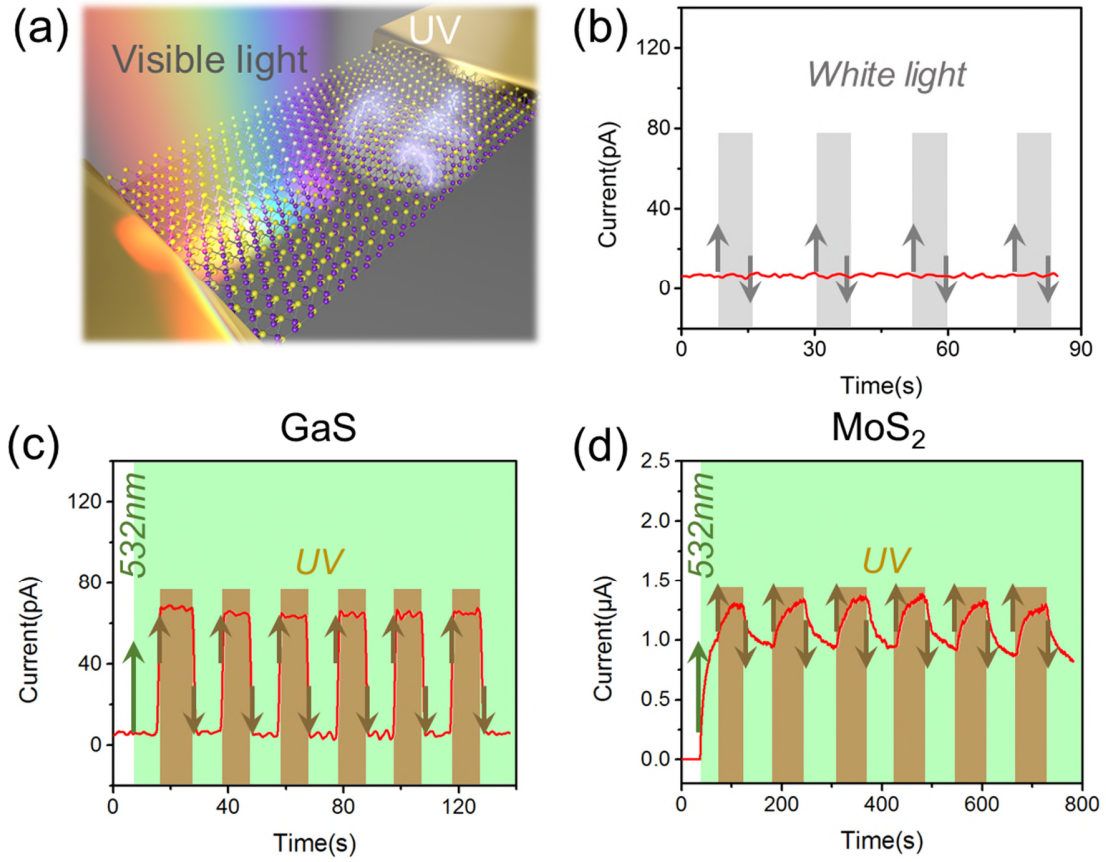


Figure 7. Application of GaS devices in information encoding by UV light: (a) Schematic illustration of UV-discriminating response in GaS optoelectronic devices. (b) I-t curve of GaS thin film devices response to white light LED ($1.35 \text{ mW}/\text{cm}^2$, 400-700 nm). (c) I-t curve of GaS thin film devices response to UV light ($65 \mu\text{W}/\text{cm}^2$) under green laser background ($9.2 \mu\text{W}$, $5 \mu\text{m}$ spot size). (d) I-t curve of MoS_2 thin film devices response to UV light under green laser background.

Conclusions

In summary, we presented a detailed study of the layer-dependent synthesis, characterization, degradation behavior and device performance of the defective $\text{GaS}_{0.87}$ and stoichiometric GaS. Large area and uniform films of 1–4 layer thickness with good controllability are synthesized by

CVD and the stoichiometry is controlled by the ratio of absorbed reactive species. The two crystals share a lot of similarity under various characterizations, with stoichiometric GaS showing much stronger light-matter interactions. Enhanced stability and UV-discriminating photoresponse was observed in stoichiometric GaS while the defective GaS_{0.87} showed photoresponse to certain visible wavelength. By using XPS and ADF-STEM, we found that the photo-induced degradation of defective GaS_{0.87} is related to sulfur vacancies and absorbed O₂, and it oxides the 2D crystal into amorphous Ga₂O₃, which then serves as encapsulation for protection of further degradation. Interestingly, the defective GaS_{0.87} is stable without exposure to strong light, and it could provide a good platform to study the effect of large amount of defects. Finally, the stoichiometric GaS was used in fabrication of large-scale high-performance device arrays for information encoding with UV-discriminating sensitivity, showing a 26-times increase of signal-to-noise ratio under visible light background than MoS₂ devices. These findings provide a thorough study (from atomic-scale structures to large-scale device performances) of the stability of GaS crystals, and demonstrate that pristine 2D GaS crystals are stable in ambient conditions and could be used in high performance sensors, photodetectors, photoswitches and short-wavelength LEDs.

Experimental Methods

Synthesis of 2D GaS films by CVD method:

A home-built two-furnace CVD system with 1-inch quartz tube was used for separate temperature control of gallium sulfide precursor and sulfur. For a typical synthesis, 10 mg gallium (III) sulfide (Ga₂S₃, powder, ≥99%, Sigma-Aldrich) was placed in the center of Furnace II. The growth substrate was cleaned in acetone and isopropanol for 15 min each, and placed downstream at the desired temperature zone. For synthesis of stoichiometric GaS crystals, 20 mg sulfur (S, powder,

$\geq 99.5\%$, Sigma-Aldrich) was put in the center of Furnace I. The synthesis parameters for various 2D GaS films have been provided in detail. For samples directly grown on TEM SiN grid, monolayer graphene film was first grown on copper film by CVD and transferred onto SiN grid via the wet transfer method described by our previous reports.⁵⁵ The precursor temperature was 830 °C and grid temperature was set at 625 °C.

Characterization of GaS_{0.87} and GaS films:

Hitachi S-4300 and ZEISS EVO was used for SEM characterization with accelerating voltage of 3.0 kV. EDX was carried out in Zeiss Merlin field emission analytical SEM with Oxford instruments Xmax 150 EDX detector. XPS was characterized in a Thermo K-alpha XPS instrument with monochromatic Al K α radiation (12 kV, 3 mA). Raman analysis was conducted in LabRam Aramis Raman spectrometer system, using 532 nm laser with $\times 50$ objective lens and spot size of $\sim 1 \mu\text{m}$. AFM analysis was performed on Asylum Research MFP-3D in AC mode with a silicon Tap300-G cantilever (BudgetSensors, spring constant $\sim 40 \text{ N/m}$ and resonant frequency $\sim 300 \text{ kHz}$) and processed by Gwyddion software. ADF-STEM imaging was conducted using Oxford's JEOL ARM-200 cold field emission gun transmission electron microscope with a Cs probe corrector and 100 mm² Centurion EDX detector under an accelerating voltage of 80 kV.

Device fabrication and measurement:

The electrodes were patterned directly on the GaS films by JEOL 5500 FS EBL system using bilayer PMMA resist and developed in MIBK/IPA solution. After that, 80 nm Au was deposited by thermal evaporation, followed by lift-off in acetone. The current was measured using a Keithley 2400 sourcemeter with two tungsten tips. For photocurrent measurements, a number of light sources with different wavelengths and focused spot sizes were used, including 275 nm deep-UV LED (Thorlab M275L4, spot size $\sim 200 \mu\text{m}$), white round LED (RS components, C503D-WAN,

spot size $\sim 300\ \mu\text{m}$), 532 nm diode-pumped solid-state laser (Thorlabs, DJ532-40, spot size $\sim 5\ \mu\text{m}$) and other unmounted visible LEDs (Thorlabs, spot size $\sim 300\ \mu\text{m}$). Power values of various light sources were recorded by a manually fixated power meter (Thorlab Optics PM100D, wavelength 200 nm–1000 nm) placed at the position of device. All measurements were carried out under room temperature in ambient conditions. Monolayer MoS_2 crystals were synthesized and characterized by the same methods we described in previous reports.⁵⁶

Supporting Information

Figure S1-S13: Additional AFM, SEM, Raman data of $\text{GaS}_{0.87}$, GaS and Ga_2S_3 ; Photoresponse time of GaS; I–t curve of $\text{GaS}_{0.87}$ devices under weak UV light; Additional SEM, Raman characterization of $\text{GaS}_{0.87}$ films after degradation; SEM, OM, Raman and PL characterization of monolayer MoS_2 devices; Basic electronic and optoelectronic characterization of MoS_2 FET devices. Table S1. Device performance of other UV-discriminating photodetectors.

Reference

- [1] Novoselov K. S., Geim A. K., Morozov S. V., Jiang D., Zhang Y., Dubonos S. V., Grigorieva I. V., Firsov A. A. Electric Field Effect in Atomically Thin Carbon Films. *Science* **2004**, *306*, 666-669.
- [2] Radisavljevic B., Radenovic A., Brivio J., Giacometti V., Kis A. Single-Layer MoS_2 Transistors. *Nat. Nanotechnol.* **2011**, *6*, 147-150.
- [3] Novoselov K. S., Mishchenko A., Carvalho A., Castro Neto A. H. 2D Materials and van der Waals Heterostructures. *Science* **2016**, *353*, aac9439.
- [4] Zhao W., Ghorannevis Z., Chu L., Toh M., Kloc C., Tan P.-H., Eda G. Evolution of Electronic Structure in Atomically Thin Sheets of WS_2 and WSe_2 . *ACS Nano* **2013**, *7*, 791-797.
- [5] Pospischil A., Furchi M. M., Mueller T. Solar-Energy Conversion and Light Emission in an Atomic Monolayer p–n Diode. *Nat. Nanotechnol.* **2014**, *9*, 257.
- [6] Jin H., Guo C., Liu X., Liu J., Vasileff A., Jiao Y., Zheng Y., Qiao S.-Z. Emerging Two-Dimensional Nanomaterials for Electrocatalysis. *Chem. Rev.* **2018**, *118*, 6337-6408.

- [7] Autere A., Jussila H., Dai Y., Wang Y., Lipsanen H., Sun Z. Nonlinear Optics with 2D Layered Materials. *Adv. Mater.* **2018**, *30*, 1705963.
- [8] Yi F., Ren H., Shan J., Sun X., Wei D., Liu Z. Wearable Energy Sources Based on 2D Materials. *Chem. Soc. Rev.* **2018**, *47*, 3152-3188.
- [9] Wang X., Cui Y., Li T., Lei M., Li J., Wei Z. Recent Advances in the Functional 2D Photonic and Optoelectronic Devices. *Adv. Opt. Mater.* **2019**, *7*, 1801274.
- [10] Gong C., Zhang X. Two-Dimensional Magnetic Crystals and Emergent Heterostructure Devices. *Science* **2019**, *363*, eaav4450.
- [11] Zhang W., Wang Q., Chen Y., Wang Z., Wee A. T. S. Van der Waals Stacked 2D Layered Materials for Optoelectronics. *2D Mater.* **2016**, *3*, 022001.
- [12] Özçelik V. O., Azadani J. G., Yang C., Koester S. J., Low T. Band Alignment of Two-Dimensional Semiconductors for Designing Heterostructures with Momentum Space Matching. *Phys. Rev. B* **2016**, *94*, 035125.
- [13] Castellanos-Gomez A. Why all the fuss about 2D semiconductors? *Nat. Photonics* **2016**, *10*, 202.
- [14] Xia F., Wang H., Xiao D., Dubey M., Ramasubramaniam A. Two-Dimensional Material Nanophotonics. *Nat. Photonics* **2014**, *8*, 899.
- [15] Late D. J., Liu B., Luo J., Yan A., Matte H. S. S. R., Grayson M. , Rao C. N. R., Dravid V. P. GaS and GaSe Ultrathin Layer Transistors. *Adv. Mater.* **2012**, *24*, 3549-3554.
- [16] Luxa J., Wang Y., Sofer Z., Pumera M. Layered Post-Transition-Metal Dichalcogenides (X-M-M-X) and Their Properties. *Chem. Eur. J.* **2016**, *22*, 18810.
- [17] Jung C. S., Shojaei F., Park K., Oh J. Y., Im H. S., Jang D. M., Park J., Kang H. S., Red-to-Ultraviolet Emission Tuning of Two-Dimensional Gallium Sulfide/Selenide. *ACS Nano* **2015**, *9*, 9585-9593
- [18] Li X., Tao L., Chen Z., Fang H., Li X., Wang X., Xu J.-B., Zhu H. Graphene and Related Two-Dimensional Materials: Structure-Property Relationships for Electronics and Optoelectronics. *Appl. Phys. Lett.* **2017**, *4*, 021306.
- [19] Hu P., Wang L., Yoon M., Zhang J., Feng W., Wang X., Wen Z., Idrobo, J. C., Miyamoto, Y., Geohegan D. B., Xiao K. Highly Responsive Ultrathin GaS Nanosheet Photodetectors on Rigid and Flexible Substrates. *Nano Lett.* **2013**, *13*, 1649-1654.
- [20] Yang S., Li Y., Wang X., Huo N., Xia J.-B., Li S.-S., Li J. High Performance Few-Layer GaS Photodetector and its Unique Photo-Response in Different Gas Environments. *Nanoscale* **2014**, *6*, 2582-2587.
- [21] Wang X., Sun Y., Liu K.. Chemical and Structural Stability of 2D Layered Materials. *2D Mater.* **2019**, *6*, 042001.
- [22] Li Q., Zhou Q., Shi L., Chen Q., Wang J. Recent Advances in Oxidation and Degradation Mechanisms of Ultrathin 2D Materials under Ambient Conditions and their Passivation Strategies. *J. Mater. Chem. A* **2019**, *7*, 4291-312.
- [23] Gao J., Li B., Tan J., Chow P., Lu T.-M., Koratkar N. Aging of Transition Metal Dichalcogenide Monolayers. *ACS Nano* **2016**, *10*, 2628-2635.
- [24] Longo R. C., Addou R., Kc S., Noh J.-Y., Smyth C. M., Barrera D., Zhang C., Hsu J. W. P., Wallace R. M., Cho K. Intrinsic Air Stability Mechanisms of Two-Dimensional Transition Metal Dichalcogenide Surfaces: Basal versus Edge Oxidation. *2D Mater.* **2017**, *4*, 025050.
- [25] Novoselov K. S., Jiang D., Schedin F., Booth T. J., Khotkevich V. V., Morozov S. V., Geim A. K. Two-Dimensional Atomic Crystals. *PNAS* **2005**, *102*, 10451-10453.
- [26] Carlsson J. M., Hanke F., Linic S., Scheffler M. Two-Step Mechanism for Low-Temperature Oxidation of Vacancies in Graphene. *Phys. Rev. Lett.* **2009**, *102*, 166104.
- [27] Yang S., Cai H., Chen B., Ko C., Özçelik V. O., Ogletree D. F., White C. E., Shen Y., Tongay S. Environmental Stability of 2D Anisotropic Tellurium Containing Nanomaterials: Anisotropic to Isotropic Transition. *Nanoscale* **2017**, *9*, 12288-12294.

- [28] Molle A., Grazianetti C., Chiappe D., Cinquanta E., Cianci E., Tallarida G., Fanciulli M. Hindering the Oxidation of Silicene with Non-Reactive Encapsulation. *Adv. Funct. Mater.* **2013**, 23, 4340-4344.
- [29] Xia W, Hu W, Li Z, Yang J. A First-Principles Study of Gas Adsorption on Germanene. *Phys. Chem. Chem. Phys.* **2014**, 16, 22495-22498.
- [30] Favron A., Gaufrès E., Fossard F., Phaneuf-L'Heureux A. -L., Tang N. Y. W., Lévesque P. L., Loiseau A., Leonelli R., Francoeur S., Martel R. Photooxidation and Quantum Confinement Effects in Exfoliated Black Phosphorus. *Nat. Mater.* **2015**, 14, 826.
- [31] Island J. O., Steele G. A., van der Zant H. S. J., Castellanos-Gomez A. Environmental Instability of Few-Layer Black Phosphorus. *2D Mater.* **2015**, 2, 011002.
- [32] Shcherbakov D., Stepanov P., Weber D., Wang Y., Hu J., Zhu Y., Watanabe K., Taniguchi T., Mao Z., Windl W., Goldberger J., Bockrath M., Lau C. N. Raman Spectroscopy, Photocatalytic Degradation, and Stabilization of Atomically Thin Chromium Tri-iodide. *Nano Lett.* **2018**, 18, 4214-4219.
- [33] Susoma J., Lahtinen J., Kim M., Riikonen J., Lipsanen H. Crystal Quality of Two-Dimensional Gallium Telluride and Gallium Selenide Using Raman Fingerprint. *AIP Adv.* **2017**, 7, 015014.
- [34] Zhao Q., Frisenda R., Gant P., Perez de Lara D., Munuera C., Garcia-Hernandez M., Niu Y., Wang T., Jie W., Castellanos-Gomez A. Toward Air Stability of Thin GaSe Devices: Avoiding Environmental and Laser-Induced Degradation by Encapsulation. *Adv. Funct. Mater.* **2018**, 28, 1805304.
- [35] Wang X., Sheng Y., Chang R.-J., Lee J. K., Zhou Y., Li S., Chen T., Huang H., Porter B. F., Bhaskaran H., Warner J. H. Chemical Vapor Deposition Growth of Two-Dimensional Monolayer Gallium Sulfide Crystals Using Hydrogen Reduction of Ga₂S₃. *ACS Omega* **2018**, 3, 7897-7903.
- [36] Zhou J., Shi J., Zeng Q., Chen Y., Niu L., Liu F., Yu T., Suenaga K., Liu X., Lin J. InSe Monolayer: Synthesis, Structure and Ultra-High Second-Harmonic Generation. *2D Mater.* **2018**, 5, 025019.
- [37] Gan X., Zhao C., Hu S., Wang T., Song Y., Li J., Zhao Q.-H., Jie W.-Q., Zhao J.-L. Microwatts Continuous-Wave Pumped Second Harmonic Generation in Few- and Mono-layer GaSe. *Light Sci. Appl.* **2018**, 7, 17126.
- [38] Jia T., Fuh H., Chen D., Abid M., Abid M., Zhang D., Sarker A. B., Cho J., Choi M., Chun B. S., Xu H., Coileain C. O., Liu H., Chang C.-R., Wu H.-C. Giant and Linear Piezo-Phototronic Response in Layered GaSe Nanosheets. *Adv. Electron. Mater.* **2018**, 4, 1700447.
- [39] Antonius G., Qiu D. Y., Louie S. G. Orbital Symmetry and the Optical Response of Single-Layer MX Monochalcogenides. *Nano Lett.* **2018**, 18, 1925-1929.
- [40] Yang Z., Jie W., Mak C.-H., Lin S., Lin H., Yang X., Yan F., Lau S. P., Hao J. Wafer-Scale Synthesis of High-Quality Semiconducting Two-Dimensional Layered InSe with Broadband Photoresponse. *ACS Nano* **2017**, 11, 4225-4236.
- [41] Yan F., Zhao L., Patane A., Hu P., Wei X., Luo W., Zhang D., Lv Q., Feng Q., Shen C., Chang K., Eaves L., Wang K. Fast, Multicolor Photodetection with Graphene-Contacted p-GaSe/n-InSe van der Waals Heterostructures. *Nanotechnology* **2017**, 28, 27LT01.
- [42] Late D. J., Liu B., Matte H., Rao C. N. R., Dravid V. P. Rapid Characterization of Ultrathin Layers of Chalcogenides on SiO₂/Si Substrates. *Adv. Funct. Mater.* **2012**, 22, 1894-1905.
- [43] Aldalbahi, A., Li, E., Rivera, M., Velazquez R., Altalhi T., Peng X., Feng P. A New Approach for Fabrications of SiC Based Photodetectors. *Sci. Rep.* **2016**, 6, 23457.
- [44] Butun, B., Tut T., Ulker E., Yelboga T., Ozbay E. High-Performance Visible-Blind GaN-Based p-i-n Photodetectors. *Appl. Phys. Lett.* **2008**, 92, 033507.
- [45] Nasiri, N., Bo R., Wang F., Fu L., Tricoli A. Ultraporous Electron-Depleted ZnO Nanoparticle Networks for Highly Sensitive Portable Visible-Blind UV Photodetectors. *Adv. Mater.* **2015**, 27, 4336-4343.
- [46] Liu, J., Lu R., Xu G., Wu J., Thapa P., Moore D. Development of a Seedless Floating Growth Process in Solution for Synthesis of Crystalline ZnO Micro/Nanowire Arrays on Graphene:

- Towards High-Performance Nanohybrid Ultraviolet Photodetectors. *Adv. Funct. Mater.* **2013**, *23*, 4941-4948.
- [47] Wang, Z., Wang H., Liu B., Qiu W., Zhang J., Ran S., Huang H., Xu J., Han H., Chen D., Shen G. Transferable and Flexible Nanorod-Assembled TiO₂ Cloths for Dye-Sensitized Solar Cells, Photodetectors, and Photocatalysts. *ACS Nano* **2011**, *5*, 8412-8419.
- [48] Kong, W.-Y., Wu G.-A., Wang K.-Y., Zhang T.-F., Zou Y.-F., Wang D.-D., Luo L.-B. Graphene- β -Ga₂O₃ Heterojunction for Highly Sensitive Deep UV Photodetector Application. *Adv Mater.* **2016**, *28*, 10725-10731.
- [49] Li, F., Meng Y., Dong R., Yip S., Lan C., Kang X., Wang F., Chan K.S. Ho J.C. High-Performance Transparent Ultraviolet Photodetectors Based on InGaZnO Superlattice Nanowire Arrays. *ACS Nano* **2019**, *13*, 12042-12051.
- [50] Ishikawa T., Ikoma H. X-Ray Photoelectron Spectroscopic Analysis of the Oxide of GaAs. *Jpn. J. Appl. Phys.* **1992**, *31*, 3981.
- [51] Catalán-Gómez S., Briones M., Redondo-Cubero A., Palomares F. J., Nucciarelli F., Lorenzo E., Pau J. L. The Role of the Oxide Shell in the Chemical Functionalization of Plasmonic Gallium Nanoparticles. *Proc. of SPIE* **2017**, *10231*, 102310D-1.
- [52] Li X., Basile L., Huang B., Ma C., Lee J. W., Vlassiounk I. V., Poretzky A. A., Lin M.-W., Yoon M., Chi M., Idrobo J. C., Rouleau C. M., Sumpter B. G., Geohegan D. B., Xiao K. Van der Waals Epitaxial Growth of Two-Dimensional Single-Crystalline GaSe Domains on Graphene. *ACS Nano* **2015**, *9*, 8078-8088.
- [53] Dickey M. D., Emerging Applications of Liquid Metals Featuring Surface Oxides. *ACS Appl. Mater. Interfaces* **2014**, *6*, 18369-18379.
- [54] Scharmann F., Cherkashinin G., Breternitz V., Knedlik C., Hartung G., Weber T., Schaefer J. A. Viscosity effect on GaInSn studied by XPS. *Surf. Interface Anal.* **2004**, *36*, 981-985.
- [55] Sheng Y., Rong Y., He Z., Fan Y., Warner J. H. Uniformity of Large-Area Bilayer Graphene Grown by Chemical Vapor Deposition. *Nanotechnology* **2015**, *26*, 395601.
- [56] Lu Y., Chen T., Ryu G. H., Huang H., Sheng Y., Chang R.-J., Warner J. H. Self-Limiting Growth of High-Quality 2D Monolayer MoS₂ by Direct Sulfurization Using Precursor-Soluble Substrates for Advanced Field-Effect Transistors and Photodetectors. *ACS Appl. Nano Mater.* **2019**, *2*, 369-378.